Journal of Physics and Chemistry of Solids 211 (2026) 113502

Contents lists available at ScienceDirect

Journal of Physics and Chemistry of Solids

journal homepage: www.elsevier.com/locate/jpcs

Effectiveness of three distinct strategies of constructing ZnO-based composites for enhanced electrochemical performance

Shujin Hao [a,1], Bo Zhang [a,1], Qingye Zhang [a], Meng Sun [a], Rongsheng Cai [b,*], Feiyu Diao [c,**], Yiqian Wang [a,***]

[a] College of Physics, Qingdao University, No. 308 Ningxia Road, Qingdao, 266071, PR China
[b] State Key Laboratory of Solid Lubrication, Lanzhou Institute of Chemical Physics, Chinese Academy of Sciences, Lanzhou, 730000, PR China
[c] Industrial Research Institute of Nonwovens & Technical Textiles, Shandong Center for Engineered Nonwovens, College of Textiles & Clothing, Qingdao University, No. 308 Ningxia Road, Qingdao, 266071, PR China

ARTICLE INFO

Keywords:
Carbon nanofibers
ZnO-based composite anode materials
Electrospinning
Electrochemical properties

ABSTRACT

Recently, constructing hybrid composite systems has emerged as a pivotal approach to optimizing the electrochemical performance of transition-metal-oxide-based anodes in lithium-ion batteries (LIBs). Common strategies involve compositing transition metal oxides with metal oxides, carbon materials (particularly carbon nanofibers, CNFs), or metals. However, no definitive consensus has been reached regarding the superiority of any single strategy. To evaluate the effectiveness of various strategies, we employ zinc oxide (ZnO) as primary material and elementary nickel (Ni) or oxide as supplementary components to fabricate three distinct ZnO-based composite anodes *via* electrospinning: (i) NiO/ZnO nanofibers, (ii) NiO/ZnO@CNFs and (iii) Ni/ZnO@CNFs. A comprehensive examination has been conducted to investigate the microstructure and electrochemical properties of these hybrid composite anode materials. It demonstrates that the Ni/ZnO@CNFs electrode exhibits the best cycling and rate performance. Notably, at a current density of 1.0 A g^{-1}, Ni/ZnO@CNFs electrode maintains a discharge specific capacity of 536.1 mAh g^{-1} after 300 cycles, with a capacity retention of 84.3 %. This is attributed to the synergistic interaction among three different components: ZnO provides a high capacity (978 mAh g^{-1}); Ni and CNFs improve the electrical conductivity of the anode material, and CNFs alleviate volume expansion during cycling. This study offers new perspectives for designing high performance transition-metal-oxide-based anodes in LIBs.

1. Introduction

As an anode material for lithium-ion batteries (LIBs), transition metal oxides (TMOs) exhibit an excellent theoretical specific capacity due to their unique lithium storage mechanism based on conversion reactions [1–3]. However, during the charging and discharging processes, TMOs-based anode materials are inevitably restricted by large volume change and poor electrical conductivity, which consequently leads to relatively poor cycling stability and rate performance [4,5]. Thus, exploring reliable strategies to optimize their electrochemical performance remains a big challenge.

Recently, establishing two- or three-component hybrid composite systems has become an important way to improve the electrochemical performance of TMOs-based anodes in LIBs [6,7]. Typical strategies involve compositing TMOs with one or two following materials: (i) metal oxides, (ii) carbon materials (particularly carbon nanofibers, CNFs), (iii) metallic materials. Among the TMOs, ZnO exhibits higher theoretical specific capacity (978 mAh g^{-1}) due to its unique lithium storage mechanism, *i.e.* conversion-alloying reactions, which has been widely applied in TMOs-based anodes [8–10]. For instance, Guo et al. [11] prepared NiO/ZnO core-shell nanorod composite, which significantly enhanced the discharge specific capacity compared to pure ZnO. Similarly, Yoon et al. [12] synthesized SnO_2/ZnO@CNF composite, which demonstrated excellent cycling stability. Additionally, Liu et al.

* Corresponding author.
** Corresponding author.
*** Corresponding author.
E-mail addresses: rongshengcai@licp.cas.cn (R. Cai), fydiao@qdu.edu.cn (F. Diao), yqwang@qdu.edu.cn (Y. Wang).
[1] These authors contributed to this work equally.

https://doi.org/10.1016/j.jpcs.2025.113502
Received 16 November 2025; Received in revised form 16 December 2025; Accepted 26 December 2025
Available online 31 December 2025

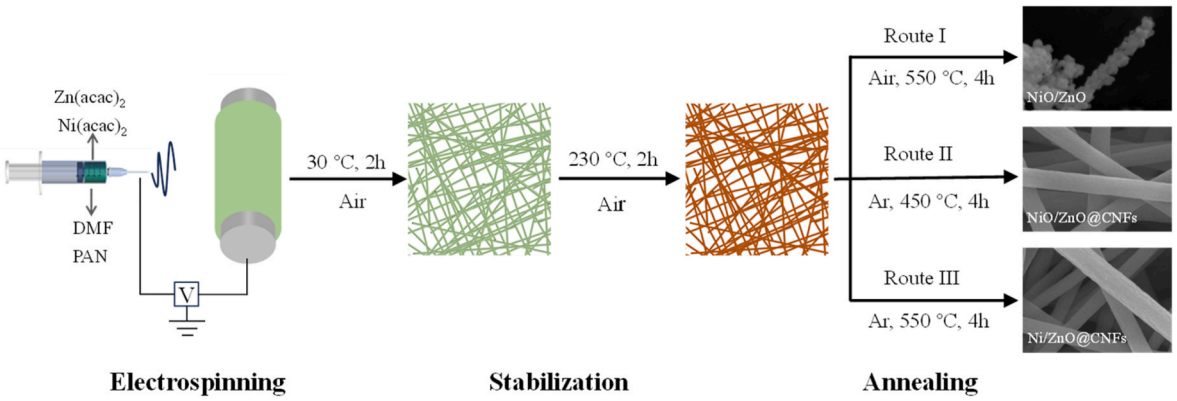

Fig. 1. Schematic illustration of the preparation processes for hybrid composites using different routes.

[13] reported the effectiveness of Co/ZnO/nitrogen-doped porous carbon composite anodes, which exhibited a discharge capacity of 411 mAh g^{-1} after 100 cycles at a current density of 0.2 A g^{-1}. All the above strategies have tried to construct two- or three-component hybrid composite systems, aiming to enhance the electrochemical properties of ZnO through the synergistic effects of different components in the composite. However, each strategy has its own advantages and limitations. For the first strategy, compositing ZnO with other metal oxides, the other metal oxides can increase the capacity of LIBs, while metal oxides generally suffer from low electrical conductivity and poor rate performance [14,15]. For the second strategy, compositing ZnO with CNFs, CNFs can alleviate the volume expansion of ZnO during cycling and enhance the electrical conductivity of the composite, but incorporating carbon (372 mAh g^{-1}) into the anode will lead to a reduction in its specific capacity [16–20]. For the third strategy, compositing ZnO with metallic particles, the catalytic metal particles can facilitate the charging/discharging process, while this composite typically demands relatively intricate preparation process such as precise combination and uniform dispersion of multiple phases [21–24]. Overall, although constructing hybrid composites can improve the electrochemical performance, no consensus has been reached about the preeminence of any single strategy.

In this work, we employed ZnO as the primary material and elementary Ni or nickel oxide as the supplementary component to fabricate three distinct ZnO-based composites *via* electrospinning, and investigated their electrochemical performances as anodes for LIBs. Among them, Ni/ZnO@CNFs exhibited the best cycling stability and rate performance, delivering a discharge specific capacity of 536.1 mAh g^{-1} after 300 cycles at a current density of 1.0 A g^{-1}, with a capacity retention rate of 84.3 %.

2. Experimental

2.1. Materials

Polyacrylonitrile (PAN, average Mw. 150,000) was employed as the carbon source, and the sources of Ni and Zn were provided by nickel acetylacetonate [$Ni(acac)_2$, 98 %] and zinc acetylacetonate [$Zn(acac)_2$, 95 %]. N, N-dimethylformamide (DMF, 99.5 %) was used as the solvent and purchased from Sinopharm Chemical Reagent Company Limited. All the chemicals used were not subjected to any further purification.

2.2. Preparation process of hybrid composites

First, $Ni(acac)_2$ and $Zn(acac)_2$ were dissolved in a DMF solution containing PAN (11 wt%) at a molar ratio of 1:2, followed by stirring for 6 h to prepare the precursor solution. Then the solution was electrospun into fiber membranes, and detailed electrospinning parameters can be found in the supplementary material. Subsequently, the fiber membranes were dried at 25 °C for 2 h, and pre-oxidized at 230 °C for 2 h in air. Afterwards, annealing treatments under different conditions were conducted to get desirable products. Route I involved annealing in air at 550 °C for 4 h to produce NiO/ZnO nanofibers; Route II utilized annealing in argon at 450 °C for 4 h to prepare CNFs loaded with NiO/ZnO nanoparticles; Route III employed annealing in argon at 550 °C for 4 h to obtain CNFs embedded with Ni/ZnO nanoparticles. The annealing conditions were determined based on systematic XRD analysis. Fig. S1 presents the XRD patterns of the products under different annealing conditions. The preparation processes with different routes are illustrated in Fig. 1.

2.3. Materials characterization

The crystal structure of the as-prepared fiber membranes was analyzed by X-ray diffractometer (XRD, Bruker D8 Advance) with Cu-Kα radiation (λ = 1.5406 Å). Then, the morphologies of the products were observed by field-emission scanning electron microscope (FE-SEM, Sigma 500) operated at 20 kV. High-angle annular dark field (HAADF) imaging *via* scanning-transmission electron microscope (STEM, Thermo Fisher Spectra 300) was conducted. Bright field (BF) and high-resolution transmission electron microscopy (HRTEM) images were acquired with a transmission electron microscope (TEM, JEOL JEM 2100F) operated at 200 kV. The valence states of the elements were determined by X-ray photoelectron spectroscopy (XPS, Thermo Scientific K-Alpha$^+$). Graphitization of CNFs was investigated by Raman spectroscopy using a confocal Raman spectrometer (Renishaw inVia) with a laser wavelength of 532 nm. Nitrogen adsorption-desorption measurements (BELSORP MaxII) were carried out to determine the specific surface area and pore structure of the composites.

2.4. Measurement of electrochemical properties

The fiber membranes produced by different routes were processed for electrode fabrication and subsequent electrochemical tests. To guarantee the fairness of performance comparison, we adopted the same preparation procedure for the electrodes obtained from different routes. All the products from different routes were first ground into powder and mixed with acetylene black and polyvinylidene fluoride in a 7:2:1 mass ratio to ensure a homogeneous mixture. N-Methylpyrrolidone (NMP) was then added as a solvent, and the mixture was ground to form a slurry. This slurry was uniformly coated onto copper foil, dried in vacuum for 12 h, and pressed into electrode sheets. Finally, all the electrodes prepared by different routes were assembled into CR2025 button batteries in an argon-filled atmosphere. A lithium sheet served as the counter electrode, while the electrolyte was composed of 1 mol/L $LiPF_6$ dissolved in a 1:1:1 (volume ratio) mixed solvent of ethylene carbonate

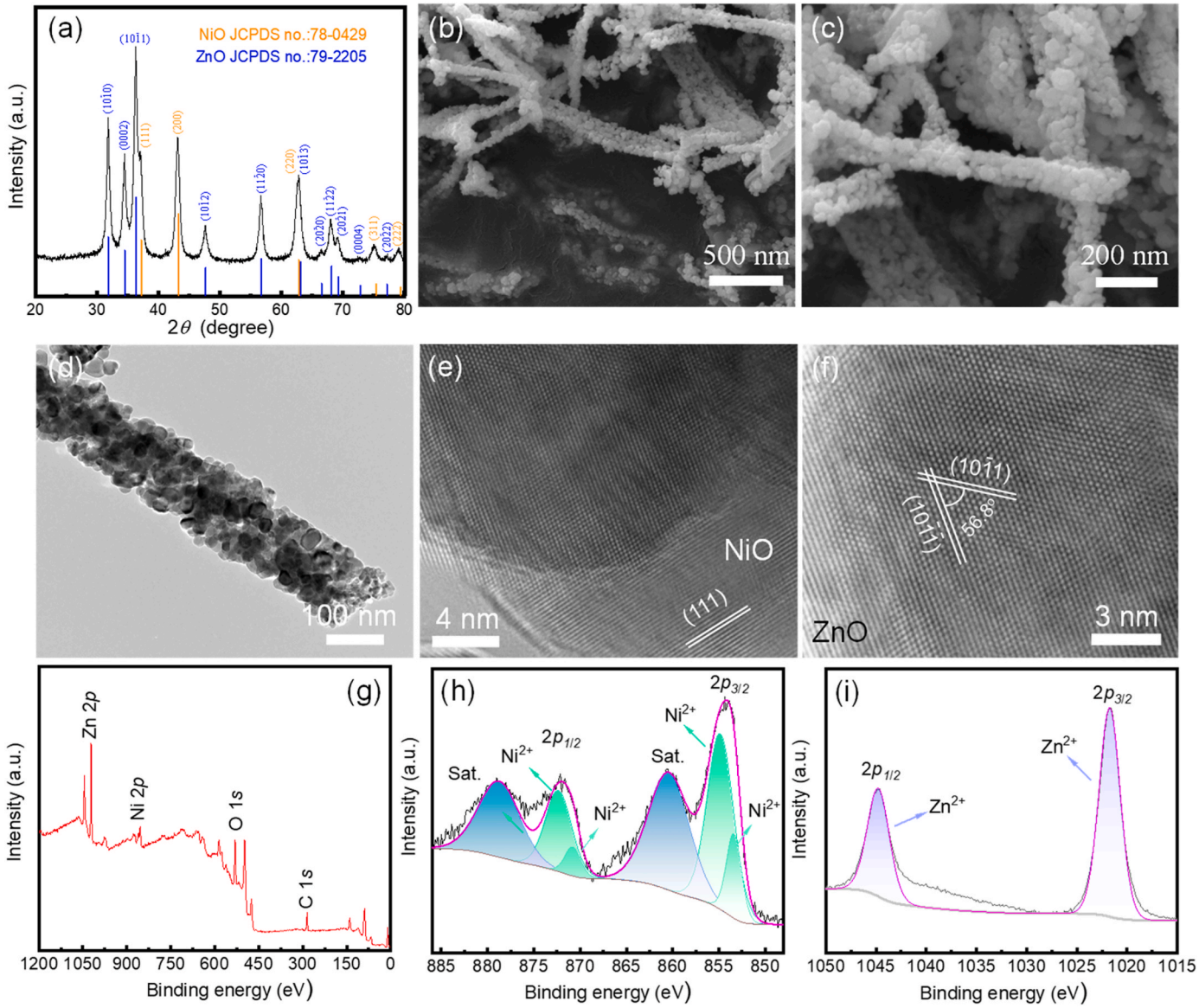

Fig. 2. Structural and microstructural characterization of NiO/ZnO: (a) XRD pattern, (b) and (c) FE-SEM images, (d) BF TEM image, (e) and (f) HRTEM images. XPS spectra: (g) Full XPS spectrum, (h) XPS spectra of Ni 2*p*, and (i) XPS spectra of Zn 2*p*.

(EC)/diethyl carbonate (DEC)/dimethyl carbonate (DMC). The cyclic voltammetry (CV) of the electrode materials was carried out using a Metrohm Autolab electrochemical workstation (PGSTAT 302 N). The cycling and rate performances were evaluated with a LAND testing system with a voltage range from 0.01 V to 3.00 V. Electrochemical impedance spectroscopy (EIS) was performed on the electrochemical workstation in an open-circuit state, with a frequency range from 100 kHz to 0.01 Hz and an interference amplitude of 5 mV.

3. Results and discussion

3.1. Structure, morphology and microstructure of NiO/ZnO

Fig. 2(a) shows the XRD pattern of the product prepared by route I. The diffraction peaks observed at 31.8°, 34.4°, 36.2°, 47.6°, 56.6°, 62.9°, 66.4°, 67.9°, 69.1°, 72.6° and 76.9° can be indexed using hexagonal ZnO ($a = 3.2501$ Å, $c = 5.2071$ Å, $\alpha = \beta = 90^{o}$ and $\gamma = 120^{o}$, JCPDS no.: 79–2205). Furthermore, the diffraction peaks at 37.2°, 43.3°, 62.9°, 75.4°, and 79.4° are attributed to NiO (JCPDS no.: 78–0429), indicating that the product is composed of ZnO and NiO [11]. Fig. 2(b) displays a morphology of nanofibers with coarse surfaces. Fig. 2(c) presents a magnified FE-SEM image of an individual fiber, revealing that the fiber is made up of nanoparticles. Fig. 2(d) shows a typical BF TEM image of the product, from which numerous voids can be found within the nanofibers, further corroborating that the fibers are formed by many nanoparticles. To gain a deeper understanding of their microstructure, a comprehensive analysis of the HRTEM images was conducted. Fig. 2(e) shows lattice fringes with a spacing of 2.41 Å and an interplanar angle of 70.5°, corresponding to the {111} planes of cubic-phase NiO [25]. Similarly, Fig. 2(f) displays lattice fringes with a spacing of 2.48 Å and an interplanar angle of 56.8°, corresponding to the {10 $\bar{1}$ 1} planes of hexagonal ZnO [26]. These TEM observations, combined with XRD analysis, provide conclusive evidence that the product is composed of NiO and ZnO nanoparticles. Fig. 2(g) shows the full XPS spectrum of the product prepared by route I. This spectrum shows a negligible amount of carbon, suggesting an absence of carbon in the product. Fig. 2(h) and (i) present the XPS spectra of Ni 2*p* and Zn 2*p*. In the Ni 2*p* spectra, the peaks observed at 873 eV and 872 eV are attributed to Ni $2p_{1/2}$ of Ni^{2+}, while the peaks at 855 eV and 853 eV correspond to Ni $2p_{3/2}$ of Ni^{2+} [27]. Additionally, the peaks at 879 eV and 861 eV are identified as

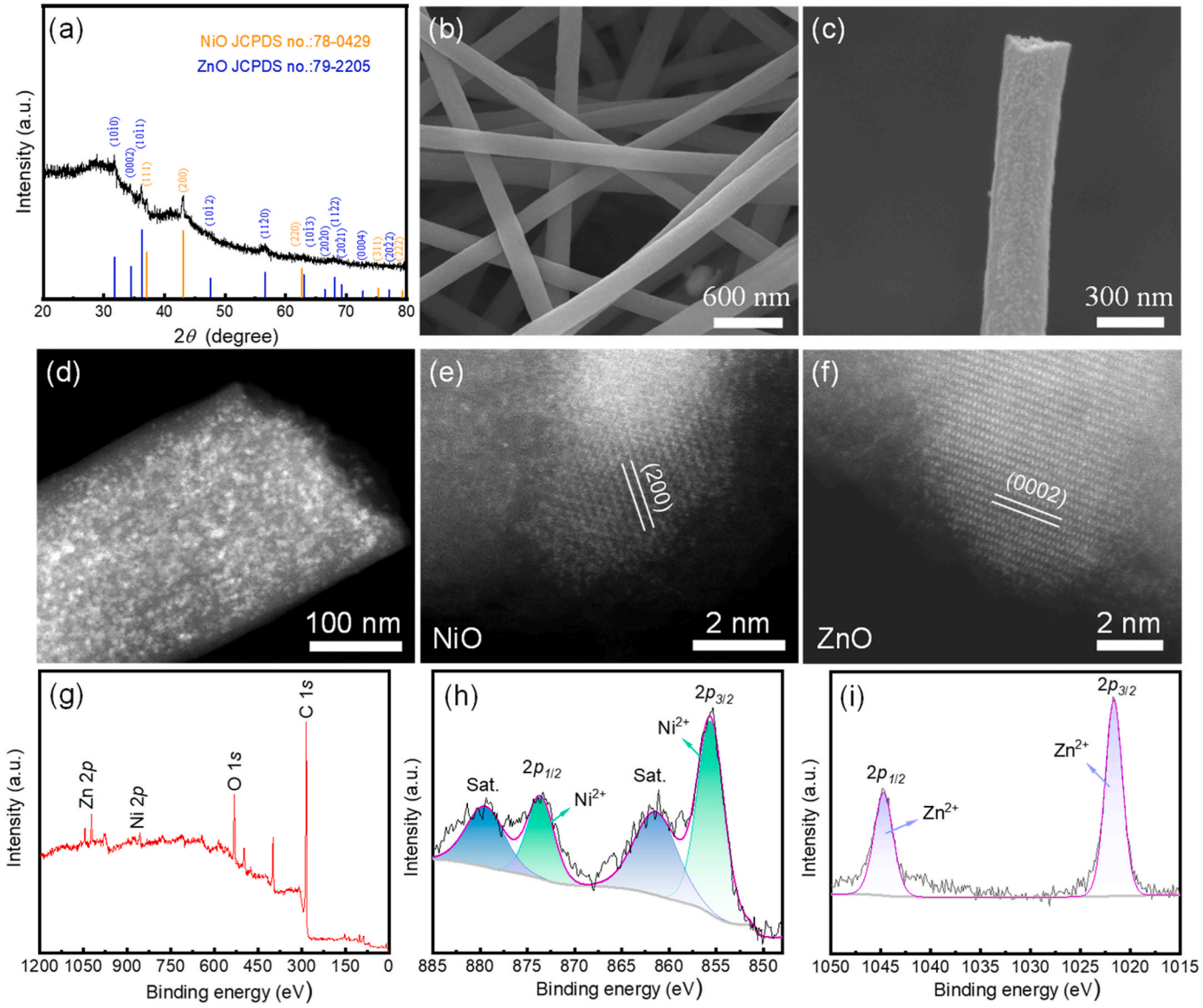

Fig. 3. Structural and microstructural characterization of NiO/ZnO@CNFs: (a) XRD pattern, (b) and (c) FE-SEM images, (d) HAADF image, (e) and (f) High-resolution STEM images. XPS spectra: (g) Full XPS spectrum, (h) XPS spectra of Ni 2*p*, (i) XPS spectra of Zn 2*p*.

satellite peaks of Ni^{2+}. In the Zn 2*p* spectrum, the peaks at 1045 eV and 1021 eV are assigned to Zn $2p_{1/2}$ and Zn $2p_{3/2}$ of Zn^{2+}, respectively [28]. From the above analysis, it is confirmed that the obtained nanofibers consist of NiO/ZnO nanoparticles.

3.2. Structure, morphology and microstructure of NiO/ZnO@CNFs

Fig. 3(a) shows the XRD pattern of the product prepared by route II. The diffraction peaks in this pattern closely match the characteristic peaks of the aforementioned NiO/ZnO nanofibers, confirming the presence of NiO and ZnO in the product. In addition, a broad peak around 30° suggests the presence of carbon in the product. Fig. 3(b) reveals that the product has a fibrous morphology with a relatively smooth surface. Fig. 3(c) presents a high-magnification FE-SEM image of an individual fiber, showing the presence of small nanoparticles on the fiber surfaces. Fig. 3(d) presents a typical HAADF image of a single nanofiber, where the nanoparticles are uniformly distributed both inside and on the surface of the nanofiber. Fig. 3(e) and (f) show typical high-resolution STEM images of nanoparticles in different regions. The lattice spacing of the particle in Fig. 3(e) is measured to be 2.08 Å, corresponding to the (200) plane of cubic NiO. In Fig. 3(f), the lattice spacing of the particle is 2.60 Å, matching the (0002) plane of hexagonal ZnO. From the above, it can be concluded that the product synthesized *via* route II consists of carbon nanofibers loaded with ZnO and NiO nanoparticles. To investigate the valence states of Ni and Zn in this composite, XPS characterization was performed. Fig. 3(g) displays a full spectrum which reveals a relatively high carbon content in the product, confirming the presence of carbon in the product. Fig. 3(h) and (i) present high-resolution XPS spectra of Ni 2*p* and Zn 2*p*, respectively. In the Ni 2*p* spectrum, the peaks located at 873 eV and 855 eV are assigned to Ni $2p_{1/2}$ and Ni $2p_{3/2}$ of Ni^{2+}, respectively, while the peaks at 879 eV and 861 eV are identified as satellite peaks of Ni^{2+}. In the Zn 2*p* spectrum, the peaks at 1045 eV and 1021 eV correspond to Zn $2p_{1/2}$ and Zn $2p_{3/2}$ of Zn^{2+}, respectively. The XPS results further confirm the presence of ZnO, NiO, and carbon in the product, indicating the formation of NiO/ZnO@CNFs.

3.3. Structure, morphology and microstructure of Ni/ZnO@CNFs

Fig. 4(a) presents the XRD pattern of the product prepared *via* route

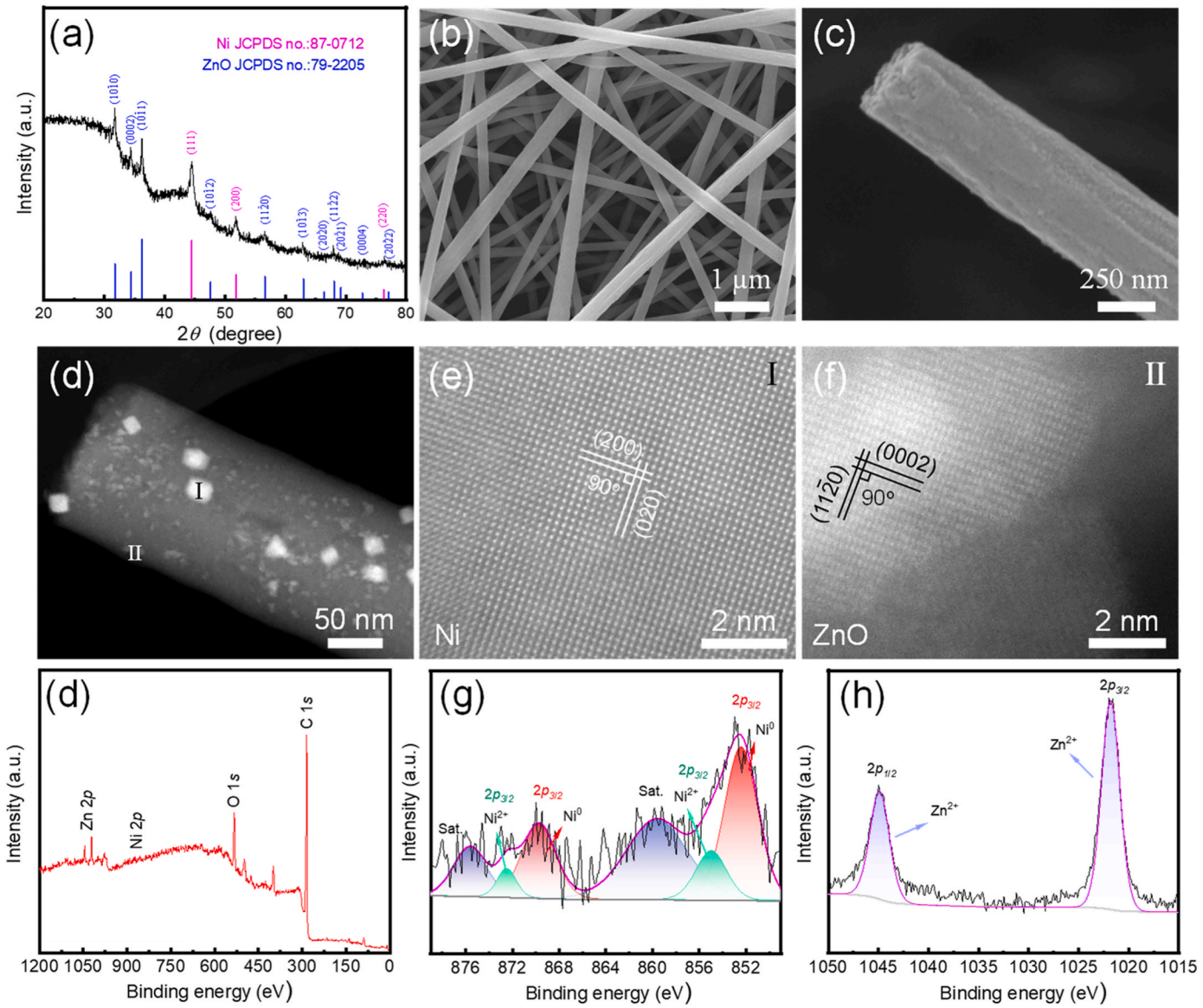

Fig. 4. Structural and microstructural characterization of Ni/ZnO@CNFs: (a) XRD pattern, (b) and (c) FE-SEM images, (d) HAADF image, (e) and (f) High-resolution STEM images. XPS spectra: (g) Full XPS spectrum, (h) XPS spectra of Ni 2*p*, (i) XPS spectra of Zn 2*p*.

III. In this pattern, the diffraction peaks observed at 44.5°, 34.4°, 51.8° and 76.4° can be indexed using cubic Ni (JCPDS no.: 87–0712, a = 3.5238 Å), and the remaining diffraction peaks can be assigned to hexagonal ZnO (JCPDS no.: 79–2205). Due to the annealing treatment conducted in Ar atmosphere, NiO is prone to be reduced into metallic nickel by carbon in the fibers at a relatively low temperature. In addition, a broad peak at around 30° confirms the presence of carbon in the product. Thus, the composition of the product is determined to be Ni, ZnO, and carbon. Fig. 4(b) indicates a fibrous morphology and a relatively smooth surface of the product, similar to that of NiO/ZnO/CNFs. Fig. 4(c) presents a typical high-magnification FE-SEM image of an individual fiber, demonstrating presence of numerous nanoparticles on the fiber surface. STEM was employed to further investigate the microstructure of the nanofibers. Fig. 4(d) shows a typical HAADF image of a single nanofiber, clearly indicating the presence of particles both inside the nanofiber and on its surface. Fig. 4(e) and (f) display high-resolution STEM images of the nanoparticles in different regions. In Fig. 4(e), the spacing of the lattices in particle I is measured to be 2.08 Å and the interplanar angle is 90°, corresponding to the {100} crystal planes of cubic Ni. Similarly, in Fig. 4(f), the spacings of the lattice fringes in particle II are measured to be 2.61 Å and 1.63 Å, consistent with the (0002) and (11 $\bar{2}$ 0) crystal planes of hexagonal ZnO, respectively. These observations suggest that the nanoparticles consist of Ni and ZnO. To further determine the valence states of Ni and Zn within the product prepared by route III, XPS characterization was performed. Fig. 4(g) displays a full XPS spectrum, revealing a high content of carbon in the product. Fig. 4(h) and (i) present the XPS spectra of Ni 2*p* and Zn 2*p*, respectively. In the Ni 2*p* spectrum, the peaks located at 870 eV and 852 eV correspond to metallic Ni (Ni^0). Meanwhile, two weak peaks located at 873 eV and 855 eV are observed, corresponding to Ni $2p_{1/2}$ and Ni $2p_{3/2}$ of Ni^{2+}, which result from the surface oxidation [29,30]. In the Zn 2*p* spectrum, the peaks at 1045 eV and 1021 eV correspond to Zn $2p_{1/2}$ and Zn $2p_{3/2}$ of Zn^{2+}, respectively, demonstrating the formation of ZnO. The XPS results further confirm the composition of the product is ZnO, Ni, and carbon.

To further investigate the differences of phase composition and graphitization in the three composites, Raman spectroscopy was performed. As shown in Fig. S2, the Raman spectrum of ZnO/NiO exhibits a prominent broad peak in the range of 400–580 cm^{-1}. Based on the standard Raman spectral characteristics of ZnO and NiO, this broad peak

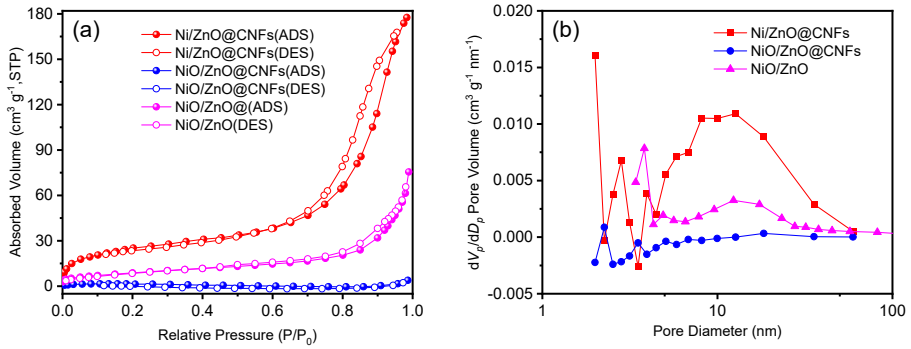

Fig. 5. (a) Nitrogen adsorption-desorption isotherms of three composites; (b) Pore size distribution curves for three composites.

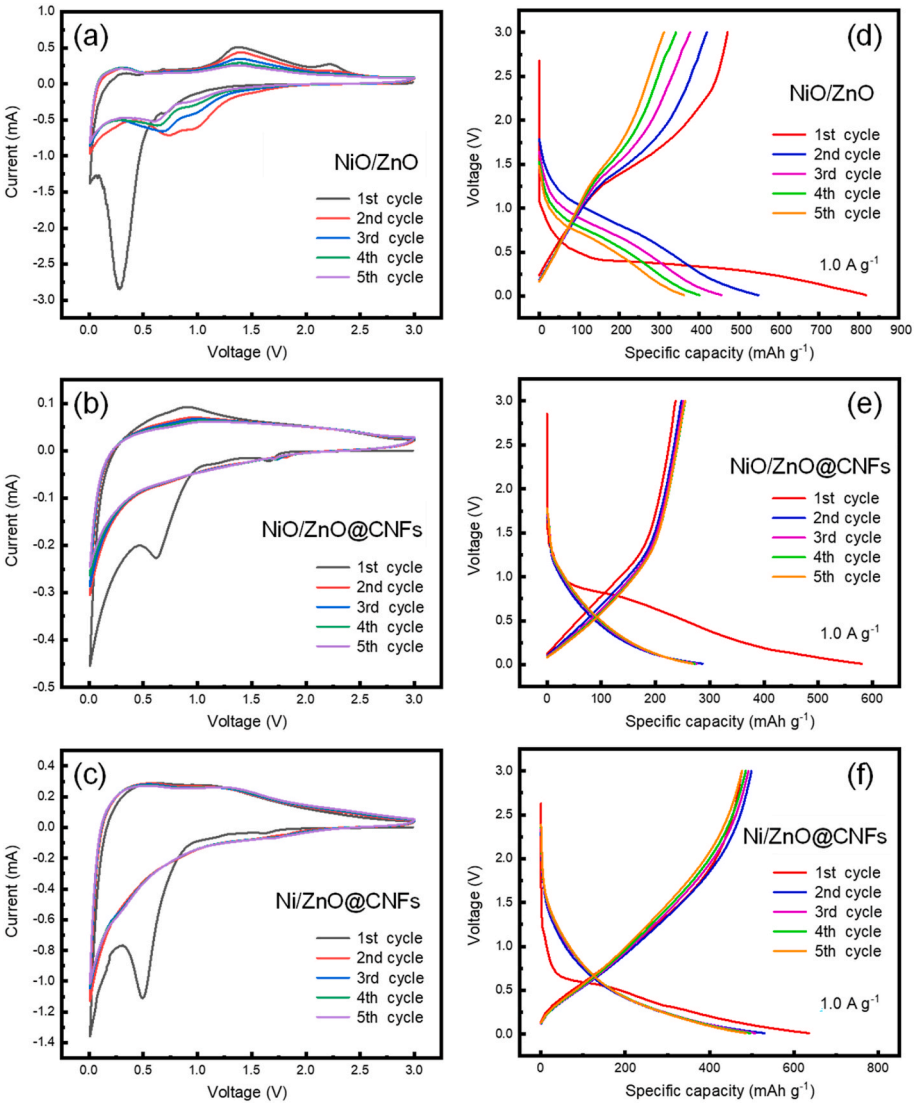

Fig. 6. CV curves of NiO/ZnO (a), NiO/ZnO@CNFs (b) and Ni/ZnO@CNFs (c) electrodes obtained at 0.3 mV s^{-1}. Voltage *versus* capacity curves of NiO/ZnO (d), NiO/ZnO@CNFs (e) and Ni/ZnO@CNFs (f) electrodes at a current density of 1.0 A g^{-1}.

originates from the overlap of their characteristic vibrational modes [31,32]. In the Raman spectra of NiO/ZnO@CNFs and Ni/ZnO@CNFs, no obvious characteristic peaks of ZnO, Ni or NiO are observed. This is ascribed to the fact that the outer carbon fibers have an extremely large Raman scattering cross-section in both NiO/ZnO@CNFs and Ni/ZnO@CNFs, and the intense signal they generate masks the signals from ZnO, NiO and Ni. [33,34]. However, two distinct characteristic peaks are found at approximately 1367 cm^{-1} and 1587 cm^{-1} in Raman spectra of both NiO/ZnO@CNFs and Ni/ZnO@CNFs, corresponding to the D and G bands of carbon, respectively. In addition, Ni/ZnO@CNFs shows lower intensity ratio of the D to G bands (I_D/I_G) than NiO/ZnO@CNFs. It is well known that a lower intensity ratio of I_D/I_G signifies a higher

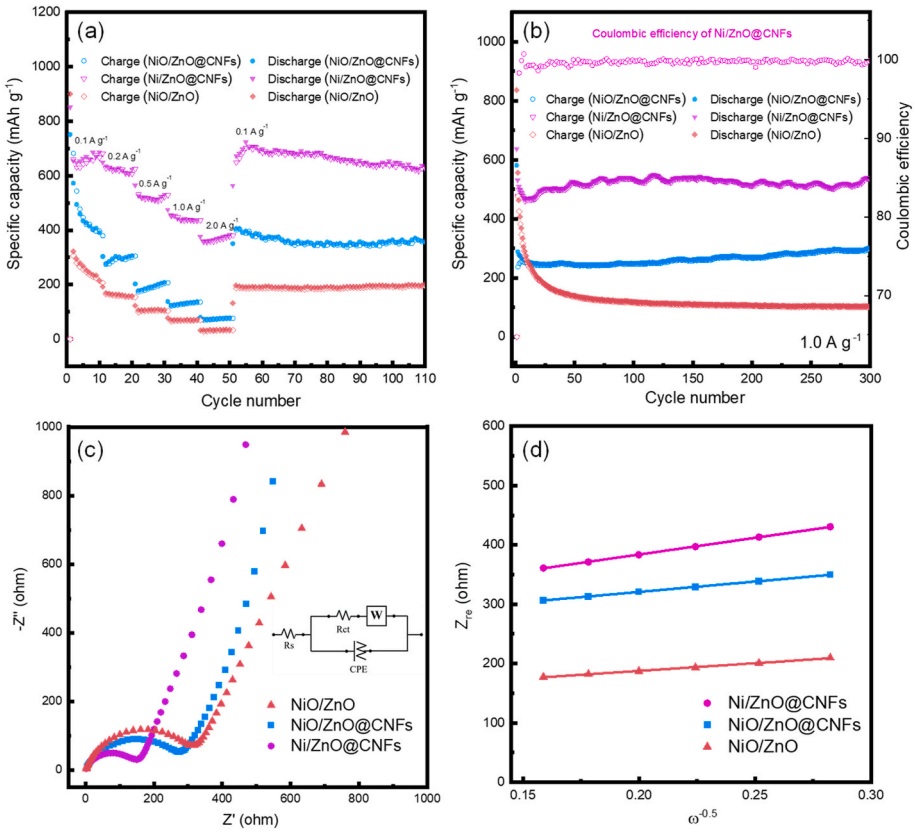

Fig. 7. (a) Rate performance of three composite electrodes at different current densities; (b) Cycling performance of three composite electrodes at a current density 1.0 A g^{-1} and Coulombic efficiency of Ni/ZnO@CNFs; (c) EIS spectra of three composite electrodes and equivalent circuit model of the EIS spectra; (d) Graph of Z^{re} plotted against $\omega^{-0.5}$ of three composite electrodes.

graphitization degree. Therefore, Ni/ZnO@CNFs has a higher graphitization degree, which is ascribed to the higher annealing temperature.

To evaluate the specific surface area and pore structure of the samples, nitrogen adsorption-desorption isotherms were tested. As presented in Fig. 5(a), according to the IUPAC classification, the isotherms of the three composites all belong to type IV, which is indicative of mesoporous materials. The specific surface areas of these composites were then calculated *via* the Brunauer-Emmett-Teller (BET). The specific surface areas are calculated to be 33.1, 6.3, and 90.4 m^2 g^{-1} for ZnO/NiO, NiO/ZnO@CNFs, and Ni/ZnO@CNFs, respectively. The Barrett-Joyner-Halenda (BJH) method was used to determine the pore size distributions of three composites. From the pore size distribution curves in Fig. 5(b), the predominant average pore diameters are determined to be 3.8 nm, 0.9 nm, and 13.1 nm for ZnO/NiO, NiO/ZnO@CNFs, and Ni/ZnO@CNFs, respectively. Combined with the TEM examinations, this is attributed to the fact that NiO is reduced into metallic Ni by carbon in the fibers under high annealing temperature, resulting in a large number of pores on the fiber surface. From the above, it can be seen that Ni/ZnO@CNFs has a larger specific surface area, which can facilitate Li-ion transport and accelerate their diffusion kinetics within the electrode.

3.4. *Electrochemical performance of NiO/ZnO, NiO/ZnO@CNFs and Ni/ZnO@CNFs electrodes*

The electrochemical performances of NiO/ZnO nanofibers, NiO/ZnO@CNFs and Ni/ZnO@CNFs electrodes were evaluated. Fig. 6 presents the CV curves of three electrodes for the first five cycles at a scan rate of 0.3 mV s^{-1}. Fig. 6(a) displays the CV curves of NiO/ZnO electrode. In the initial cathodic process, a reduction peak observed at 0.3 V corresponds to reduction of Ni^{2+} and Zn^{2+} to Ni^0 and Zn^0, formation of a solid electrolyte interphase (SEI) film on the surface of the electrode, and Li–Zn alloying reaction [35]. During the anodic process, two oxidation peaks at 1.38 V and 2.22 V are attributed to the multi-step oxidation of Zn^0/Ni^0 to Zn^{2+}/Ni^{2+} [36]. From the second to the fifth cycle, the curves do not overlap, indicating a poor cycling stability. Fig. 6(b) and (c) show typical CV curves of the NiO/ZnO@CNFs and Ni/ZnO@CNFs electrodes, where a reduction peak is found at 1.6 V in the initial cathodic process, corresponding to the insertion of Li^+ into the electrode material [37]. The strong peak observed at 0.6 V for NiO/ZnO@CNFs is attributed to the reduction of Zn^{2+} and Ni^{2+} to Zn^0 and Ni^0, while the peak observed at 0.5 V for Ni/ZnO@CNFs is ascribed to the reduction of Zn^{2+} to Zn^0. These peaks are also associated with the formation of SEI films on the surfaces of the anode materials and the Li–Zn alloying reaction. During the initial anodic process, the peak at 0.9 V (for NiO/ZnO@CNFs) corresponds to the oxidation of Zn^0 and Ni^0 to Zn^{2+} and Ni^{2+}, while the peak at 1.1 V (for Ni/ZnO@CNFs) is assigned to the oxidation of Zn^0 and Ni^0 to Zn^{2+} and Ni^{2+}. The intensity of the redox peaks for both NiO/ZnO@CNFs and Ni/ZnO@CNFs electrodes decreases from the second to the fifth cycle, which is caused by the formation of the SEI film and the irreversibility of conversion reactions for the active material. Furthermore, the CV curves show nearly complete overlap, indicating an excellent cycling stability. The electrochemical reactions involved are described by Equ. (1) to (5) [38,39] as follows.

$$ZnO + 2Li^+ + 2e^- \leftrightarrow Zn + Li_2O \quad (1)$$

$$NiO + 2Li^+ + 2e^- \leftrightarrow Ni + Li_2O \quad (2)$$

$$Zn + Li^+ + e^- \leftrightarrow LiZn \quad (3)$$

$$Zn + Li_2O \leftrightarrow ZnO + 2Li^+ + 2e^- \quad (4)$$

$$Ni + Li_2O \leftrightarrow NiO + 2Li^+ + 2e^- \quad (5)$$

Table 1
Specific capacities and capacity retention rates for three composite anodes.

Anode materials	Initial discharge capacity at 1.0 A g^{-1} (mAh g^{-1})	Capacity after 300 cycles at 1.0 A g^{-1} (mAh g^{-1})	Capacity retention rate
NiO/ZnO	835.5	87.5	10.5 %
NiO/ZnO@CNFs	580.4	300.4	51.8 %
Ni/ZnO@CNFs	635.9	536.1	84.3 %

Fig. 6(d–f) show initial five discharge/charge profiles of NiO/ZnO, NiO/ZnO@CNFs and Ni/ZnO@CNFs electrodes at 1.0 A g^{-1}, respectively. Upon further examination, it is found that there are significant differences in the specific discharge capacities of the three electrodes. Specifically, NiO/ZnO exhibits an initial discharge specific capacity of 835.5 mAh g^{-1} at 1.0 A g^{-1}, much higher than that of NiO/ZnO@CNFs electrode (580.4 mAh g^{-1}) and Ni/ZnO@CNFs electrode (635.9 mAh g^{-1}). This is attributed to the incorporation of carbon materials in NiO/ZnO@CNFs and Ni/ZnO@CNFs, which reduces the initial discharge capacity of the anode materials. After the first charge-discharge cycle, the capacities for all electrodes decrease, which is primarily ascribed to the formation of the SEI film. Notably, the voltage *versus* capacity curves of both NiO/ZnO@CNFs and Ni/ZnO@CNFs electrodes exhibit nearly complete overlap from the second to the fifth cycle, which demonstrates an excellent cycling stability. In contrast, the NiO/ZnO electrode shows a continuous capacity decline during the same cycling period, highlighting its inferior cycling stability. This is mainly attributed to the fact that the CNFs possess certain flexibility and structural stability, which can alleviate the stress caused by volume changes and inhibit the agglomeration of active materials, thereby improving the cycling stability of the electrode [12].

Rate performance and long-cycle stability are two crucial factors for evaluating the practical application potential of electrode materials. To assess the rate performance, the three electrodes were tested at various current densities. As shown in Fig. 7(a), the discharge capacities of the three electrodes were measured at 0.1, 0.2, 0.5, 1.0, and 2.0 A g^{-1}. Among the three electrodes, Ni/ZnO@CNFs exhibits the best rate performance, with average discharge capacities of 702.2, 624.2, 522.6, 444.4 and 368.5 mAh g^{-1} at current densities of 0.1, 0.2, 0.5, 1.0 and 2.0 A g^{-1}, respectively. When the current density is restored to 0.1 A g^{-1}, the average discharge specific capacity of Ni/ZnO@CNFs reaches 693.0 mAh g^{-1}, significantly higher than those of NiO/ZnO@CNFs and NiO/ZnO. This is due to the fact that the surface of the Ni/ZnO@CNFs composite contains a large number of mesopores, which is highly conducive to the rapid transport of ions. Ni/ZnO@CNFs has an excellent rate performance, highlighting its ability to adapt to various current conditions during charge and discharge processes. Fig. 7(b) shows the cycling performance of three electrode materials at a current density of 1.0 A g^{-1}. After 300 cycles, the specific discharge capacity of Ni/ZnO@CNFs maintains 536.1 mAh g^{-1}, which is higher than that of NiO/ZnO@CNFs (300.4 mAh g^{-1}) and NiO/ZnO (87.5 mAh g^{-1}). This discrepancy stems from the synergistic effects of different components and structural design: Ni/ZnO@CNFs exhibits superior performance primarily due to the combined advantages of metallic Ni and CNFs networks. Specifically, metallic Ni provides high electrical conductivity and excellent structural stability; the flexible CNF framework effectively buffers the volume change of ZnO, suppresses particle agglomeration, and facilitates ion/electron transport. In contrast, NiO/ZnO@CNFs suffers from significant volume expansion of NiO, weakening the interface with ZnO despite of the CNF support. For the NiO/ZnO, it lacks the CNF framework, leading to severe agglomeration, poor conductivity, and rapid capacity fading due to unmitigated volume stress. Furthermore, the initial Coulombic efficiencies (ICE) of the NiO/ZnO, NiO/ZnO@CNFs, and Ni/ZnO@CNFs electrodes are 41 %, 58 %, and 75 %, respectively. For the NiO/ZnO electrode, the surfaces of both NiO and ZnO nanoparticles are directly exposed to the electrolyte due to lack of carbon coating. Thus, NiO/ZnO electrode has poor electrical conductivity, and the charge transfer in the first cycle is uneven, leading to localized high current density and causing excessive decomposition of the electrolyte. This results in the formation of a thicker and less stable SEI film, thus leading to the lowest ICE. In contrast, NiO and ZnO nanoparticles are coated with CNFs which have good conductivity. The conductive CNFs ensure uniform charge distribution, promoting the formation of a thin and dense SEI film and reducing the irreversible consumption of lithium ions. Hence, the ICE of NiO/ZnO@CNFs electrode is higher than that of NiO/ZnO electrode. For the Ni/ZnO@CNFs, metallic Ni forms a conductive network with CNFs, significantly enhancing electron transport capability. This allows more ZnO particles to participate in reversible redox reactions during the first cycle. Consequently, Ni/ZnO@CNFs electrode exhibits the highest ICE. Table 1 summarizes the specific capacities and capacity retention rates of these three composite anodes. It can be seen that the electrodes compositing with CNFs display a higher capacity retention rate, indicating that the CNFs can effectively enhance their cycling stability.

To further investigate the electrochemical reaction kinetics, EIS tests were performed on the electrodes. Fig. 7(c) presents the EIS spectra of the NiO/ZnO, NiO/ZnO@CNFs and Ni/ZnO@CNFs electrodes, where the diameter of the semicircle at high frequencies corresponds to the charge transfer resistance of each electrode [40,41]. Moreover, the EIS data can be fitted with an equivalent circuit diagram illustrated in Fig. 7(c), with *Rs*, *Rct*, W, and CPE corresponding to electrolyte resistance, charge-transfer resistance, Warburg impedance, and constant phase element, respectively [42,43]. Upon fitting the high-frequency region, the *Rct* values of the NiO/ZnO, NiO/ZnO@CNFs and Ni/ZnO@CNFs electrodes are 366.7, 310.3 and 162.3 Ω, respectively. NiO/ZnO electrode exhibits the highest charge transfer resistance due to intrinsic limitations of transition metal oxides. NiO/ZnO@CNFs electrode shows a relatively low resistance, owing to the fact that CNFs can enhance conductivity and reduce interfacial polarization. Ni/ZnO@CNFs electrode has the lowest resistance, indicating that the metal Ni can further enhance the electrical conductivity of the electrode material. The above findings clearly highlight the synergistic effects of CNFs and Ni in optimizing charge transfer kinetics of the electrodes. In the EIS spectrum, an inclined line observed at low frequencies reflects the lithium-ion diffusion coefficient (D_{Li}) of the electrode. The value of D_{Li} can be calculated by Equ. (6) and (7) [36,37].

$$D_{Li} = \frac{R^2T^2}{2A^2n^4F^4C^2\sigma^2} \tag{6}$$

$$Z' = R_s + R_{ct} + \sigma\omega^{-0.5} \tag{7}$$

The variables in these equations are defined as follows. n is the number of electrons transferred per mole of the substance (*i.e.*, NiO, $n = 2$), C represents the concentration of lithium ions in the battery, A is the electrode area (1.54×10^{-4} m^2), F represents the Faraday constant (96485 C mol^{-1}), R is the gas constant (8.314 J K^{-1} mol^{-1}) and T is 298.15 K. Fig. 7(d) shows the fitting diagrams of Z_{re} and $\omega^{-0.5}$ for different electrodes. The σ values are calculated to be 7.4, 12.8 and 13.5 Ω $s^{-0.5}$ for NiO/ZnO, NiO/ZnO@CNFs and Ni/ZnO@CNFs electrodes, respectively. The D_{Li} values of NiO/ZnO, NiO/ZnO@CNFs and Ni/ZnO@CNFs electrodes are determined to be 4.1×10^{-16}, 1.4×10^{-16} and 1.3×10^{-16} cm^2 s^{-1}, respectively. The high D_{Li} of NiO/ZnO is attributed to its composition of nanoparticles and the presence of large voids between nanoparticles. However, significant volume expansion during cycling leads to substantial capacity fading, resulting in poor cycling performance. For the Ni/ZnO@CNFs, the better rate

Table 2
Summary of electrochemical properties for ZnO-based anode materials.

Anode materials	Cycling performance			Rate performance		Ref.
	Current density (A g^{-1})	Cycle number	Capacity (mAh g^{-1})	Current density (A g^{-1})	Capacity (mAh g^{-1})	
ZnO nanowires	0.1	100	<200	0.2	<200	[44]
				2.0	<200	
ZnO@carbon composite	0.2	200	519.3	0.4	441	[45]
				1.0	304	
ZnO/NiO core-shell nanorods	0.2	50	525	/	/	[11]
				/	/	
ZnO/Ni hollow microspheres	0.1	100	470	0.2	405	[23]
				2.0	105	
ZnO@CNFs	0.1	100	723	0.2	601	[46]
				2.0	160	
Layered ZnO@Ni microspheres	0.1	100	565	0.2	535	[47]
				1.0	315	
Ni/ZnO@CNFs	1.0	300	536.1	0.2	624.2	This work
				2.0	368.5	

performance is ascribed to the improved conductivity induced by both Ni and carbon fiber. Table 2 summarizes the electrochemical performance of ZnO-based anode materials reported in previous literature. Through comparison with other studies, it is verified that Ni/ZnO@CNFs electrode possesses excellent cycling stability and rate performance. This is attributed to the synergistic interaction among three different components: ZnO provides a high capacity (978 mAh g^{-1}); CNFs alleviate volume expansion during cycling, while Ni and CNFs can improve the electrical conductivity of the anode material.

4. Conclusions

In this work, ZnO has been employed as the primary material and elementary Ni or oxide as the supplementary component to fabricate three distinct ZnO-based composite anodes by electrospinning: (i) NiO/ZnO nanofibers, (ii) NiO/ZnO@CNFs and (iii) Ni/ZnO@CNFs. Among them, the Ni/ZnO@CNFs demonstrates superior cycling stability and rate performance. At a current density of 1.0 A g^{-1}, it delivers a discharge specific capacity of 536.1 mAh g^{-1} after 300 cycles, with a capacity retention rate of 84.3 %. Moreover, its discharge capacity reaches 368.5 mAh g^{-1} at 2.0 A g^{-1}. The excellent electrochemical performance of Ni/ZnO@CNFs electrode is attributed to the synergistic interaction among three different components: ZnO provides a high capacity (978 mAh g^{-1}), Ni and CNFs improve the electrical conductivity of the anode material, and CNFs alleviate volume expansion during cycling. This work presents a promising strategy for developing high-performance LIB anode materials, thus offering a rational and adaptable pathway for designing other advanced anode materials.

CRediT authorship contribution statement

Shujin Hao: Writing – original draft, Investigation, Formal analysis. **Bo Zhang:** Investigation, Formal analysis. **Qingye Zhang:** Writing – review & editing, Formal analysis. **Meng Sun:** Formal analysis. **Rongsheng Cai:** Writing – review & editing, Formal analysis. **Feiyu Diao:** Writing – review & editing, Methodology, Formal analysis. **Yiqian Wang:** Writing – review & editing, Supervision, Funding acquisition, Conceptualization.

Declaration of competing interest

There are no conflicts to declare.

Acknowledgments

The authors gratefully acknowledge the financial support from the High-end Foreign Experts Programs, China (Grant Nos.: G2022025015L, G2022025016L, H20250033), and Shandong Province "Double-Hundred Talent Plan" Program (Grant No.: WST2018006). Y. Q. Wang acknowledges the support from the Taishan Scholar Program of Shandong Province, China, the Qingdao International Center of Semiconductor Photoelectric Nanomaterials, and the Shandong Provincial University Key Laboratory of Optoelectrical Material Physics and Devices.

Appendix A. Supplementary data

Supplementary data to this article can be found online at https://doi.org/10.1016/j.jpcs.2025.113502.

Data availability

Data will be made available on request.

References

[1] P. Poizot, S. Laruelle, S. Grugeon, L. Dupont, J.-M. Tarascon, Nano-sized transition-metal oxides as negative-electrode materials for lithium-ion batteries, Nature 407 (2000) 496–499, https://doi.org/10.1038/35035045.
[2] G. Maduraiveeran, M. Sasidharan, W. Jin, Earth-abundant transition metal and metal oxide nanomaterials: synthesis and electrochemical applications, Prog. Mater. Sci. 106 (2019) 100574, https://doi.org/10.1016/j.pmatsci.2019.100574.
[3] M.M. Thackeray, C. Wolverton, E.D. Isaacs, Electrical energy storage for transportation-approaching the limits of, and going beyond, lithium-ion batteries, Energy Environ. Sci. 5 (2012) 7854, https://doi.org/10.1039/C2EE21892E.
[4] H. Tian, A. Song, H. Tian, J. Liu, G. Shao, H. Liu, G. Wang, Single-atom catalysts for high-energy rechargeable batteries, Chem. Sci. 12 (22) (2021) 7656–7676, https://doi.org/10.1039/d1sc00716e.
[5] A. Manthiram, An outlook on lithium ion battery technology, ACS Cent. Sci. 3 (2017) 1063–1069, https://doi.org/10.1021/acscentsci.7b00288.
[6] Q. Xie, Y. Ma, X. Wang, D. Zeng, L. Wang, L. Mai, D. Peng, Electrostatic assembly of sandwich-like Ag-C@ZnO-C@Ag-C hybrid hollow microspheres with excellent high-rate lithium storage properties, ACS Nano 10 (2016) 1283–1291, https://doi.org/10.1021/acsnano.5b06650.
[7] G. Zhang, S. Hou, H. Zhang, W. Zeng, F. Yan, C.C. Li, H. Duan, High-performance and ultra-stable lithium-ion batteries based on MOF-derived ZnO@ZnO quantum dots/C core-shell nanorod arrays on a carbon cloth anode, Adv. Mater. 27 (2015) 2400–2405, https://doi.org/10.1002/adma.201405222.
[8] M. Yu, A. Wang, Y. Wang, C. Li, G. Shi, An alumina stabilized ZnO-graphene anode for lithium ion batteries via atomic layer deposition, Nanoscale 6 (2014) 11419–11424, https://doi.org/10.1039/C4NR02576H.
[9] H. Yue, Z. Shi, Q. Wang, Z. Cao, H. Dong, Y. Qiao, Y. Yin, S. Yang, MOF-derived cobalt-doped ZnO@C composites as a high-performance anode material for lithium-ion batteries, ACS Appl. Mater. Interfaces 6 (2014) 17067–17074, https://doi.org/10.1021/am5046873.
[10] V. Gurylev, T.P. Perng, Defect engineering of ZnO: review on oxygen and zinc vacancies, J. Eur. Ceram. Soc. 41 (2021) 4977–4996, https://doi.org/10.1016/j.jeurceramsoc.2021.03.031.
[11] J. Fang, Y. Yuan, L. Wang, H. Ni, H. Zhu, J. Gui, J. Yang, Y. Chen, S. Guo, Hierarchical ZnO@NiO core-shell nanorod array as high performance anode material for lithium-ion batteries, Mater. Lett. 111 (2013) 1–4, https://doi.org/10.1016/j.matlet.2013.08.058.
[12] B.N. Joshi, S. An, H.S. Jo, K.Y. Song, H.G. Park, S. Hwang, S.S. Al-Deyab, W. Y. Yoon, S.S. Yoon, Flexible, freestanding, and binder-free SnOx-ZnO/carbon

nanofiber composites for lithium ion battery anodes, ACS Appl. Mater. Interfaces 8 (2016) 9446–9453, https://doi.org/10.1021/acsami.6b01093.
[13] Y. Chang, C.-H. Huang, W.-R. Liu, Co/ZnO/nitrogen-doped carbon composite anode derived from metal organic frameworks for lithium ion batteries, Polymers 14 (2022) 3085, https://doi.org/10.3390/polym14153085.
[14] Z. Cui, M. Sun, H. Liu, S. Li, Q. Zhang, C. Yang, G. Liu, J. Zhong, Y.Q. Wang, Double-shell SnO_2@Fe_2O_3 hollow spheres as a high-performance anode materials for lithium-ion batteries, CrystEngComm 22 (2020) 1197–1208, https://doi.org/10.1039/C9CE01621J.
[15] X. Deng, M. Zhu, J. Ke, W. Li, D. Xiong, Z. Feng, M. He, SnO_2-ZnO nanoparticles wrapped in graphite nanosheets as a large-capacity, high-rate and long-lifetime anode for lithium-ion batteries, Chem. Phys. Lett. 769 (2021) 138392, https://doi.org/10.1016/j.cplett.2021.138392.
[16] F. Xie, X. Sheng, Z. Ling, S. Hao, Q. Zhang, M. Sun, G. Liu, F. Diao, Y.Q. Wang, Flexible electrospun iron/manganese-based compounds/carbon fibers: phase transformation and electrochemical properties, Electrochim. Acta 470 (2023) 143288, https://doi.org/10.1016/j.electacta.2023.143288.
[17] G.T. Liu, J.J. Wang, X.Y. Xue, Y.Q. Wang, Tuning the structural and magnetic properties of electrospun strontium-iron-oxide nanofibers with different stoichiometry, Mater. Char. 200 (2023) 112884, https://doi.org/10.1016/j.matchar.2023.112884.
[18] J.J. Wang, X. Sheng, S. Hao, G. Liu, R. Cai, X. Xue, Y.Q. Wang, Construction of $Fe_{0.64}Ni_{0.36}$@graphite nanoparticles via corrosion-like transformation from $NiFe_2O_4$ and surface graphitization in flexible carbon nanofibers to achieve strong wideband microwave absorption, J. Colloid Interface Sci. 657 (2024) 193–207, https://doi.org/10.1016/j.jcis.2023.11.145.
[19] S. Hao, X. Sheng, F. Xie, M. Sun, F. Diao, Y.Q. Wang, Electrospun carbon nanofibers embedded with heterostructured $NiFe_2O_4$/$Fe_{0.64}Ni_{0.36}$ nanoparticles as an anode for high-performance lithium-ion battery, J. Energy Storage 80 (2024) 110412, https://doi.org/10.1016/j.est.2023.110412.
[20] X. Sheng, T. Li, M. Sun, G. Liu, Q. Zhang, Z. Ling, S. Gao, F. Diao, J. Zhang, F. Rosei, Y.Q. Wang, Flexible electrospun iron compounds/carbon fibers: phase transformation and electrochemical properties, Electrochim. Acta 407 (2022) 139892, https://doi.org/10.1016/j.electacta.2022.139892.
[21] M.T. Ahmed, H. Abdullah, Y.X. Qiu, D.H. Kuo, Enhancing hydrogen evolution reaction efficiency with electrospun Ni-doped Zn (O, S) microfibers photocatalyst: a novel approach for sustainable energy conversion, Int. J. Hydrogen Energy 95 (2024) 784–795, https://doi.org/10.1016/j.ijhydene.2024.11.244.
[22] H. Wu, L. Wei, W. Li, C. Shi, X. Yao, Q. Fu, H. Li, X. Guo, Highly conductive carbon/carbon composites as advanced multifunctional anode materials for structural lithium-ion batteries, Adv. Funct. Mater. 34 (2024) 2403729, https://doi.org/10.1002/adfm.202403729.
[23] S. Shen, W. Zhong, X. Huang, Y. Lin, T. Wang, Ordered ZnO/Ni hollow microsphere arrays as anode materials for lithium ion batteries, Materials 12 (2019) 1193, https://doi.org/10.3390/ma12071193.
[24] Q. Xie, Y. Ma, X. Zhang, L. Wang, G. Yue, D. Peng, ZnO/Ni/C composite hollow microspheres as anode materials for lithium ion batteries, J. Alloys Compd. 619 (2015) 235–239, https://doi.org/10.1016/j.jallcom.2014.08.240.
[25] X. Wen, K. Xie, Regulating lattice oxygen on the surfaces of porous single-crystalline NiO for stabilized and enhanced CO oxidation, Catalysts 14 (2024) 130, https://doi.org/10.3390/catal14020130.
[26] C. Parvathiraja, S. Shailajha, G. Abinaya, S. Shanavas, M.S.K. Mubina, R. Acevedo, Modified polymer network gel preparation on Ag/ZnO quasi sphere nanostructure with enhanced structural and optical properties, Mater. Res. Express 6 (2019) 0950a2, https://doi.org/10.1088/2053-1591/ab337b.
[27] R.S. Yadav, I. Kuřitka, J. Vilcakova, J. Havlica, J. Masilko, L. Kalina, J. Tkacz, V. Enev, M. Hajdúchová, Structural, magnetic, dielectric, and electrical properties of $NiFe_2O_4$ spinel ferrite nanoparticles prepared by honey-mediated sol-gel combustion, J. Phys. Chem. Solid. 107 (2017) 150–161, https://doi.org/10.1016/j.jpcs.2017.04.004.
[28] J.G. Kim, Y. Kim, Y. Noh, W.B. Kim, Formation of carbon-coated ZnFe2O4 nanowires and their highly reversible lithium storage properties, RSC Adv. 4 (2014) 27714–27721, https://doi.org/10.1039/C4RA02095B.
[29] Y. Xu, X. Liu, S. Wang, Z. Fu, L. Sun, W. Feng, Z. Lv, Y. Cui, X. Li, P. Yin, A. DeMerle, E. Burcar, Z. Wang, Z. Yang, A mechanical strategy of surface anchoring to enhance the electrochemical performance of ZnO/$NiCo_2O_4$@nickel foam self-supporting anode for lithium-ion batteries, Adv. Compos. Hybrid Mater. 7 (2024) 238, https://doi.org/10.1007/s42114-024-01058-3.
[30] N.P. Klochko, K.S. Klepikova, I.I. Tyukhov, Y.O. Myagchenko, E.E. Melnychuk, V. R. Kopach, G.S. Khrypunov, V.M. Lyubov, A.V. Kopach, V.V. Starikov, M. V. Kirichenko, Zinc oxide-nickel cermet selective coatings obtained by sequential electrodeposition, Sol. Energy 117 (2015) 1–9, https://doi.org/10.1016/j.solener.2015.03.047.
[31] S.K. Vemuri, S. Khanna, Utsav, S. Paneliya, V. Takhar, R. Banerjee, I. Mukhopadhyay, Fabrication of silver nanodome embedded zinc oxide nanorods for enhanced Raman spectroscopy, Colloids Surf., A 639 (2022) 128336, https://doi.org/10.1016/j.colsurfa.2022.128336.
[32] Y. Song, S.X. Zhang, C.H. Zhang, Y.T. Yang, K.Y. Lv, Raman spectra and microstructure of zinc oxide irradiated with swift heavy ion, Crystals 9 (2019) 395, https://doi.org/10.3390/cryst9080395.
[33] M. Lashanizadegan, Z. Bedoreh, F. Mousavi, Synthesis, characteristics, adsorption and catalytic behavior of NiO-ZnO-CdO/reduced graphene oxide nanocomposites, ChemistrySelect 8 (2023) e202301670, https://doi.org/10.1002/slct.202301670.
[34] M.M. Hossain, H. Shima, Md A. Islam, M. Hasan, M. Lee, Synergetic effect in Raman scattering of ZnO nanoparticles in ZnO-CNT fibers: a way to enhance the G and 2D band, J. Phys. Chem. C 120 (2016) 17670–17682, https://doi.org/10.1021/acs.jpcc.6b03484.
[35] C.J. Pelliccione, Y. Ding, E.V. Timofeeva, C.U. Segre, In situ XAFS study of the capacity fading mechanisms in ZnO anodes for lithium-ion batteries, J. Electrochem. Soc. 162 (2015) A1935–A1939, https://doi.org/10.1149/2.1011509jes.
[36] Y. Huang, X. Chen, K. Zhang, X. Feng, Preparation of graphene supported flower-like porous 3D ZnO-NiO ternary composites for high capacity anode materials for Li-ion batteries, Ceram. Int. 41 (2015) 13532–13540, https://doi.org/10.1016/j.ceramint.2015.07.147.
[37] H. Savitha, N. Kottam, C. Sampath, G.M. Madhu, C.S. Aishwarya, Recent advances in cost-effective ZnO-based electrode material for lithium-ion batteries, ChemistrySelect 9 (2024) e202402489, https://doi.org/10.1002/slct.202402489.
[38] Z. Cui, Q. Xie, A. Manthiram, Zinc-doped high-nickel, low-cobalt layered oxide cathodes for high-energy-density lithium-ion batteries, ACS Appl. Mater. Interfaces 13 (2021) 15324–15332, https://doi.org/10.1021/acsami.1c01824.
[39] L. Wang, G. Zhang, Q. Liu, H. Duan, Recent progress in Zn-based anodes for advanced lithium ion batteries, Mater. Chem. Front. 2 (2018) 1414–1435, https://doi.org/10.1039/C8QM00125A.
[40] B. Zhang, F. Xie, S.J. Hao, M. Sun, F.Y. Diao, R.S. Cai, Y.Q. Wang, Effect of annealing atmosphere on the phase composition and electrochemical properties of iron-oxide-based electrospun nanofibers, J. Energy Storage 124 (2025) 116851, https://doi.org/10.1016/j.est.2025.116851.
[41] G. Yu, X. Liu, W. Huang, S. Wang, J. Zhan, L. Ma, H. Li, X. Lin, T. Liu, K. Amine, H. Li, Ferromagnetic atomic d-p orbital hybridization for promoting Al-S batteries, Adv. Mater. (2025) 2418784, https://doi.org/10.1002/adma.202418784.
[42] F. Xie, M. Sun, X.L. Sheng, Q.Y. Zhang, Z.B. Ling, S.J. Hao, F.Y. Diao, Y.Q. Wang, Graphene-wrapped Fe_2TiO_5 nanoparticles with enhanced performance as lithium-ion battery anode, Mater. Lett. 358 (2024) 135877, https://doi.org/10.1016/j.matlet.2024.135877.
[43] L.S. Zhang, F. Xie, S.J. Hao, F.Y. Diao, Y.Q. Wang, Annealing condition engineering of electrospun iron-titanium oxide nanofibers for enhanced lithium storage performance, Electrochim. Acta 536 (2025) 146746, https://doi.org/10.1016/j.electacta.2025.146746.
[44] D. Kim, S.H.R. Shin, Y. Kim, K. Crossley, H. Han, J. Yoo, Hierarchical assembly of ZnO nanowire trunks decorated with ZnO nanosheets for lithium ion battery anodes, RSC Adv. 10 (2020) 13655–13661, https://doi.org/10.1039/D0RA00372G.
[45] J. Zhang, R. Ding, F. Li, Z. Tian, Y. Lu, ZIF-8-derived ultrasmall ZnO nanoparticles embedded in porous carbon nanocage as anode material for lithium-ion batteries, Ionics 30 (2024) 5215–5224, https://doi.org/10.1007/s11581-024-05655-6.
[46] W. Wang, W. Qiu, Y. Zhang, X. Wang, Facile synthesis of free-standing nanorod structured ZnO@carbon nanofiber film and its application in lithium-ion battery anode, Solid State Sci. 109 (2020) 106430, https://doi.org/10.1016/j.solidstatesciences.2020.106430.
[47] H. Yang, L. Chang, L. Wang, D. Yin, D. Wang, Y. Cheng, Binder-free layered ZnO@Ni microspheres as advanced anode materials for lithium-ion batteries, Ionics 26 (2020) 3281–3288, https://doi.org/10.1007/s11581-019-03424-4.